2016

Binder-free and carbon-free 3D porous air electrode for Li-O2 batteries with high efficiency, high capacity, and long life

Wenbin Luo
University of Wollongong, wl368@uowmail.edu.au

Xuanwen Gao
University of Wollongong, xg973@uowmail.edu.au

Dongqi Shi
University of Wollongong, dongqi@uow.edu.au

Shulei Chou
University of Wollongong, shulei@uow.edu.au

Jiazhao Wang
University of Wollongong, jiazhao@uow.edu.au

See next page for additional authors

Publication Details

Luo, W., Gao, X., Shi, D., Chou, S., Wang, J. & Liu, H. (2016). Binder-free and carbon-free 3D porous air electrode for Li-O2 batteries with high efficiency, high capacity, and long life. Small, 12 (22), 3031-3038.

Binder-free and carbon-free 3D porous air electrode for Li-O2 batteries with high efficiency, high capacity, and long life

Abstract
Pt-Gd alloy polycrystalline thin film is deposited on 3D nickel foam by pulsed laser deposition method serving as a whole binder/carbon-free air electrode, showing great catalytic activity enhancement as an efficient bifunctional catalyst for the oxygen reduction and evolution reactions in lithium oxygen batteries. The porous structure can facilitate rapid O2 and electrolyte diffusion, as well as forming a continuous conductive network throughout the whole energy conversion process. It shows a favorable cycle performance in the full discharge/charge model, owing to the high catalytic activity of the Pt-Gd alloy composite and 3D porous nickel foam structure. Specially, excellent cycling performance under capacity limited mode is also demonstrated, in which the terminal discharge voltage is higher than 2.5 V and the terminal charge voltage is lower than 3.7 V after 100 cycles at a current density of 0.1 mA cm−2. Therefore, this electrocatalyst is a promising bifunctional electrocatalyst for lithium oxygen batteries and this depositing high-efficient electrocatalyst on porous substrate with polycrystalline thin film by pulsed laser deposition is also a promising technique in the future lithium oxygen batteries research.

Keywords
capacity, efficiency, high, batteries, o2, li, electrode, air, porous, 3d, carbon, life, free, long, binder

Disciplines
Engineering | Physical Sciences and Mathematics

Publication Details
Luo, W., Gao, X., Shi, D., Chou, S., Wang, J. & Liu, H. (2016). Binder-free and carbon-free 3D porous air electrode for Li-O2 batteries with high efficiency, high capacity, and long life. Small, 12 (22), 3031-3038.

Authors
Wenbin Luo, Xuanwen Gao, Dongqi Shi, Shulei Chou, Jiazhao Wang, and Hua-Kun Liu

DOI: 10.1002/((please add manuscript number))
Article type: Full paper

Binder-free and carbon-free 3D porous air electrode for Li-O_2 batteries with high efficiency, high capacity, and long life

Wen-Bin Luo, Xuan-Wen Gao, Dong-Qi Shi, Shu-Lei Chou, Jia-Zhao Wang*, Hua-Kun Liu*

W. B. Luo, Dr. X.W. Gao, Dr. S. D. Shi, Dr. S. L. Chou, Prof. J. Z. Wang, Prof. H.K. Liu
Institute for Superconducting and Electronic Materials, University of Wollongong, Wollongong, NSW 2522 Australia

E-mail: shulei@uow.edu.au

Keywords: Li-O_2 battery; oxygen reduction reaction; polycrystalline thin film; PtGd alloy; pulsed laser deposition;

Two-dimensional Pt-Gd alloy polycrystalline thin film was deposited on three-dimensional nickel foam by pulsed laser deposition method serving as a whole binder/carbon-free air electrode, showing great catalytic activity enhancement as an efficient bifunctional catalyst for the oxygen reduction and evolution reactions in lithium oxygen batteries. The porous structure can facilitate rapid O_2 and electrolyte diffusion, as well as forming a continuous conductive network throughout the whole energy conversion process. It shows a favorable cycle performance in the full discharge/charge model, owing to the high catalytic activity of the Pt-Gd alloy composite and three-dimensional porous nickel foam structure. Specially, excellent cycling performance under capacity limited mode is also demonstrated, in which the terminal discharge voltage is higher than 2.5 V and the terminal charge voltage is lower than 3.7 V after 100 cycles at a current density of 0.1 mA cm^{-2}. Therefore, this electrocatalyst is a promising bifunctional electrocatalyst for lithium oxygen batteries and this depositing high-

efficient electrocatalyst on porous substrate with polycrystalline thin film by pulsed laser deposition is also a promising technique in the future lithium oxygen batteries research.

1. Introduction

Recently, extensive research has been devoted to the development of next generation lithium oxygen battery owing to its high theoretical energy density.[1, 2] However, it is still of great challenge to achieve high energy efficiency with lower overpotential, and satisfactory cycling performance. [3] The key to solve these problems is to efficiently combine both an appropriate porous air electrode structure and a highly active bifunctional catalyst towards the oxygen reduction reaction (ORR) and the oxygen evolution reaction (OER).[4-14] From the catalyst point of view, Pt-Gd alloy is a promising catalyst for the ORR, being the most active polycrystalline Pt-alloy reported in the literature so far.[15-17] This enhancement in activity is considerably higher than that exhibited by Pt_xNi, Pt_xCo, or Pt_xFe alloy catalyst, which also revealed several times enhancement compared to polycrystalline Pt.[17-22] Compared with other rare earth elements, such as La, Y, and Ce, Pt-Gd alloy also exhibits high kinetic catalytic activity owing to the increased compressive strain compared to these other elements in the Pt skeleton structure.[15, 17] However, to our knowledge, there is still no report using Pt-Gd alloy in lithium air battery system as eletrocatalyst. It is also difficult to optimize the specific activity of these small nanocrystals by engineering since these nanocrystals tend to agglomerate and easily detach from the carbon-based support, which will greatly hinder the catalyst activity. Therefore, it is not possible to take full advantage of the catalyst. Furthermore, the commonly used carbon-based catalyst substrate and binder, such as polyvinylidebe fluoride (PVDF), are not stable in oxygen-riched electrochemical environment in lithium oxygen battery system, surviving nucleophilic attack of high-sensitive intermediated radicals and being decomposed to LiF, LiOH and Li_2CO_3.[23-25]

Herein, in this work, we firstly deposited Pt-Gd alloy polycrystalline thin film (PTF) directly on three-dimensional (3D) porous structured cheaper substrate nickel foam by pulsed laser deposition (PLD) method serving as a whole binder/carbon-free high-activity electrode, not only suppressing the formation of irreversible byproducts but also increasing the precious metal catalyst usage effectivity. This PTF catalyst features a thin film, rather than a distribution of discrete and isolated nanoparticles. Due to the polycrystalline catalyst thin film itself and the close packed spacing of the catalyst coating on the substrate, the specific catalytic activity towards oxygen reduction is up to 10 times higher than for 2-3 nm diameter particles, in line with the kinetic activity of polycrystalline or single crystal bulk surfaces.[26-28] The thin film polycrystalline can be considered as a two-dimensional (2D) thin film array of nanocrystals, which will be even more promising for obtaining more catalytic activity from Pt-Gd alloy composite with the special polycrystalline structure. This carbon and binder-free air-electrode of Pt-Gd alloy catalyst with a polycrystalline thin film on 3D nickel foam (denoted as Ni@PG-PTF), was also firstly used as an efficient bifunctional catalyst for the ORR and OER in lithium oxygen batteries. This designed 3D porous structure can also form a continuous conductive network and improve the adsorption of and immersion in electrolyte on the surfaces of deposited Pt-Gd alloy thin film in order to facilitate the electrode reaction kinetics for high energy conversion. Meanwhile, without any carbon conductive additive and binder, this electrode can also overcome the impedance increase owing to the formation of interfacial Li_2CO_3 via the reaction of lithium peroxide with carbon. [25]

2. Result and Discussion

The morphology and phase of the as-prepared electrode with Pt-Gd alloy PTF was characterized by field emission scanning electron microscope (FESEM), high-resolution transmission electron microscopy (HRTEM) and selected area electron diffraction (SAED), as

shown in Fig. 1(a, b) and Fig. S1. The thickness of the as-obtained Pt-Gd alloy polycrystalline thin film is about 50 nm, and the electrode forms a whole 3D porous structure. The SAED patterns of Pt-Gd alloy PTF (PG-PTF) and polycrystalline Pt PTF (Pt-PTF) exhibit a similar face-centered-cubic (fcc) phase, as shown in Fig. S1. The energy dispersive X-ray spectroscopy (EDS) of Ni@PG-PTF electrode also shows a similar Pt and Gd uniform distributions in the 3D nickel foam structure as shown in Fig.S2. Information on the chemical binding from the Pt 4f signal of PG-PTF is given in Fig. S3, with the peaks deconvoluted into metallic platinum (1 and 1′) and Pt-Gd (2 and 2′) components. Individual columns of atoms and intensity variations across different columns within each particle can be detected in aberration-corrected high-angle annular dark-field (HAADF) images collected by scanning transmission electron microscopy (STEM), which reveal chemical composition variations within individual particles on the atomic scale. The HAADF intensity for each column of atoms is proportional to the product of the square of the average atomic number (Z^2) for each column of atoms and particle thickness. [18] As shown in Fig. 1c, the Pt-Gd nanoparticle thickness changes (dashed line) obtained from a truncated octahedron cannot fully account for the intensity variations (solid line) observed in Fig. 1e. Meanwhile, as for pure Pt nanoparticles, the intensity variations (solid line) observed from Fig. S4 reveal a similar trend to the thickness changes (dashed line) obtained from a truncated octahedron serving as a model of an ideal nanoparticle. It is evident that some columns of atoms close to the particle center have lower average atomic numbers than the surface regions, which suggests the formation of alloy nanoparticles that are the same as in the nanoparticle diagram in Fig. 1e. Pt and Gd show a similar distribution over the entire area, and the atomic ratio of Pt : Gd is about 3.6 (Fig. S5).

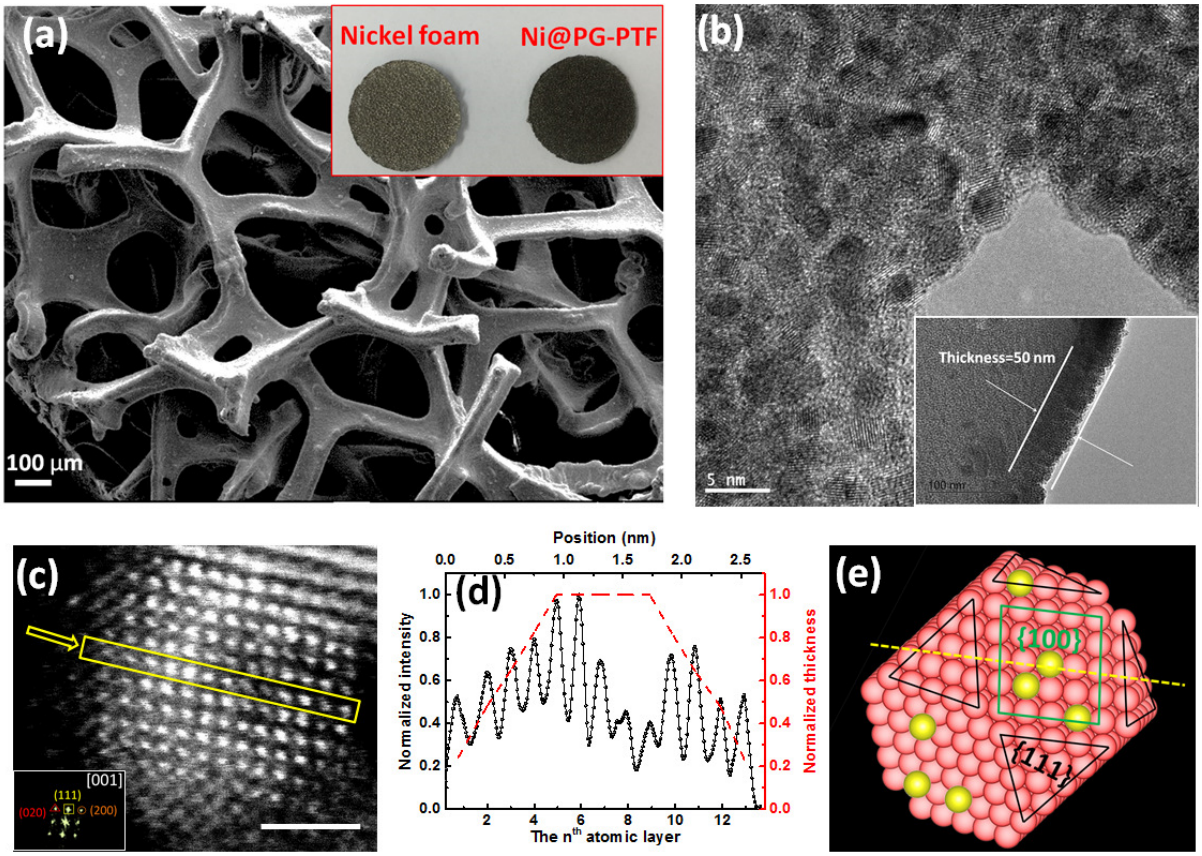

Figure 1. (a) FESEM of the air electrode (photograph of nickel foam and PG-PTF electrode); (b) HRTEM images of Pt-Gd alloy PTF, with the inset image showing the thickness of Pt-Gd alloy PTF at higher magnification; (c) aberration-corrected HAADF image of Pt-Gd nanoparticles; (d) normalized image intensity of the particles in (c) along the column outlined in yellow (solid curve), with the dashed curve the normalized thickness changes obtained by assuming the shape of the ideal nanoparticle shown in (e).

The ORR activities of PG-PTF and Pt-PTF were measured by the rotating disk electrode (RDE) technique in O_2 saturated 0.1 M KOH electrolyte at a scan rate of 10 mV s^{-1}. RDE curves at various rotation speeds were collected to determine the samples' ORR kinetic performance, as shown in Fig. S6 (Supporting Information). As shown in the RDE curves in Fig. 2(a), compared with Pt electrode and Pt-PTF, PG-PTF shows a superior ORR activity with more positive reduction peak potential and onset potential, and higher reduction current

density. The half-wave potential of an ORR polarization curve, $E_{1/2}$, is often used to evaluate the electrocatalytic activity. The onset for Pt-Gd alloy electrode starts at ~1 V, and a significant positive shift of ~120 mV was observed in the half-wave potential, implying a significant enhancement of the ORR activity. The Tafel plots of the specific activity versus measured potential (Figure 2(b)) clearly show that the ORR kinetics of PG-PTF is definitely superior to those of Pt and Pt-PTF in the range of the kinetically controlled region (0.88–0.98 V). The PG-PTF catalyst showed a smaller Tafel slope (~ 49 mV per decade) than that measured from the Pt (~ 57 mV per decade) and the Pt-PTF catalysts (~ 55 mV per decade). The enhanced kinetic current densities of the PG-PTF catalyst relative to Pt and Pt-PTF are shown in Fig. 2(c). The kinetic current densities of the PG-PTF catalyst were higher than those of the other catalysts. For example, at 0.9 V, the PG-PTF catalyst showed about 8-fold enhancement in activity compared with the Pt catalysts. This excellent ORR activity can be attributed to the alloy structure, which can lead to a shortened Pt-Pt bond distance and more catalytic activity points relative to the pure Pt nanoparticles. According to reported results, [15, 17, 19, 20, 22] the compressed Pt-Pt bond length plays a key role in decreasing the valence band center relative to the Fermi level and reducing the binding strength and/or coverage of oxygenated adsorbates, which can result in ORR activity enhancement. In an O_2 saturated non-aqueous organic system [1 M $LiCF_3SO_3$ in tetraethylene glycol dimethyl ether (TEGDME)], as shown in Fig. 2(d), the cyclic voltammogram (CV) curves of PG-PTF and P-PTF catalyst were collected. Compared with P-PTF, the PG-PTF shows obvious much earlier ORR and OER potentials and smaller over-potentials in O_2-saturated electrolyte, which indicate that PG-PTF features bifunctional catalyst performance in the anodic and cathodic scan processes in an O_2 saturated non-aqueous organic system. Generally speaking, the enhancement of oxygen catalytic activity should be result from the combination of ligand, geometric, and/or ensemble effects in the octahedral structure. This Pt-alloy skeleton-structured composite allows optimization of the surface electronic structure, weakening its

binding to the O-containing reaction intermediates and maximizing the ORR activity. [17, 20, 22, 29]

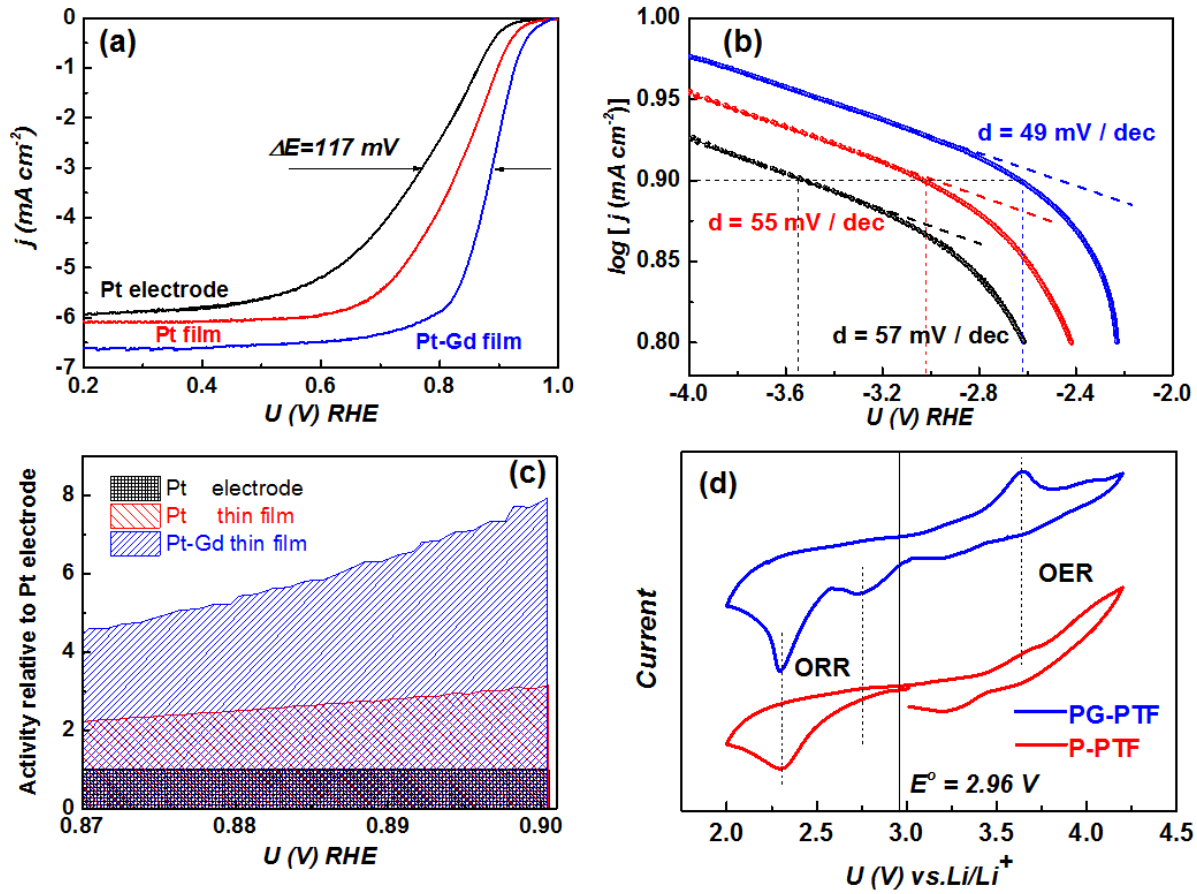

Figure 2. (a) RDE curves of Pt electrode, P-PTF, and PG-PTF; (b) Tafel slopes of Pt electrode, P-PTF, and PG-PTF, from the data shown in (a); (c) activity enhancement relative to Pt electrode (j_k/j_k^{Pt}), from the data shown in (a); (d) cyclic voltammogram curves of P-PTF and PG-PTF catalyst in a non-aqueous organic system (1 M $LiCF_3SO_3$ in TEGDME). RHE: reversible hydrogen electrode.

Finally, the binder/carbon-free air-electrode Ni@PG-PTF was used as the air electrode for Li-O_2 batteries. The electrochemical properties were then examined in a lithium oxygen cell. The full discharge and charge performances at different current densities are shown in Fig. 3a and Fig. S7. Ni@PG-PTF exhibited a low discharge-charge gap at current density of 0.05 mA cm^{-2}, which resulted in excellent round-trip efficiency (78 %) in the first full discharge/charge cycle. The charge plateau of the Ni@PG-PTF is lower than 3.6 V, which is vital for electrochemical energy storage devices. It also exhibits a high discharge specific capacity of ~ 3700 mAh g^{-1} at a current density of 0.05 mA cm^{-2}. More importantly, the

Ni@PG-PTF also shows excellent cycling performance in the full discharge/charge model at a current density of 0.05 mA cm^{-2}. After 10 cycles, Ni@PG-PTF still retains a favorable overpotential, the charge plateau is still lower than 3.7 V and the discharge capacity is still up to ~ 2700 mAh g^{-1}. When the current density is increased to 0.2 mA cm^{-2}, as shown in Fig. S8, the Ni@PG-PTF composite also exhibits good full discharge/charge cycle performance, with nearly 2000 mAh g^{-1} in the first cycle and 1400 mAh g^{-1} after 9 cycles. However, during 5 cycles full discharge/charge process at a current density of 0.05 mA cm^{-2} as shown in Fig.S7, Ni@P-PTF experience a large fall trend and higher OER potential. Compared with Ni@P-PTF, the low overpotential can be attributed from both the high synergistic catalytic activity of Pt-Gd and geometric effects from abundant surface lattice strain/defects. The high capacity results from the coral-like reaction products "grown" on the catalyst thin film, as shown in the FESEM image in Fig. 3b and HRTEM in Fig. S9. Arrays of coral-like Li_2O_2 columns with diameters in the range of 100 nm are deposited on the surface of the Ni@PG-PTF. An individual Li_2O_2 column was investigated using HRTEM and electron diffraction to determine the crystal structure and to further research the formation mechanism of the coral-like column formed in Fig. 3(c, d). In Fig. 3c, the coral-like Li_2O_2 clusters are composed of arrays of plate-like Li_2O_2 crystallites, as shown in the inset image. These Li_2O_2 platelets, roughly parallel to each other, are grown from the electrocatalyst thin film to form a layer-by-layer Li_2O_2 cluster. Additional Li_2O_2 platelets nucleated in different spaces result in the characteristic coral-like morphology observed for large particles. The electron diffraction pattern of the Li_2O_2 clusters exhibits characteristic diffraction ring signals corresponding to Li_2O_2, as shown in the Fig. 3d inset pattern. [30] Fig. 3e schematically shows the mechanism of electrochemical growth of the coral-like Li_2O_2. The first step is the reduction of O_2 on the surface of the electrocatalyst thin film to form O^{2-}, which will bind with Li^+ to form an intermediate reaction product: LiO_2*. The LiO_2* can either desorb by solvation or undergo a disproportionation reaction ($2LiO_2^* \rightarrow Li_2O_2 + O_2$) to grow on the surface of the catalyst thin film, or undergo direct

reduction with Li^+ to form nanoplatelets of Li_2O_2. [29, 30] In the following process, the obtained individual Li_2O_2 nanoplatelets are assembled layer-by-layer with nanosheet-shaped structured growth to form coral-like large particles. From the conclusions of some previous works, [7, 9, 33, 34, 35] large-scale deposition of Li_2O_2 will result in certain outcomes, including coverage of the active reaction sites due to high overpotential and blockage of the gas and electrolyte diffusion for further deposition. This porous coral-like Li_2O_2 deposition structure, however, not only contributes to facile reversibility in the charge OER process, resulting in a low overpotential, but would also be of benefit for the cycling performance. The polycrystalline electrocatalyst thin film provides enormous activity sites for Li_2O_2 formation in different orientations. The porous nickel foam, on the other hand, can facilitate rapid O_2 and electrolyte diffusion through the film, as well as forming a continuous 3D electron conductive network throughout the whole energy conversion process.

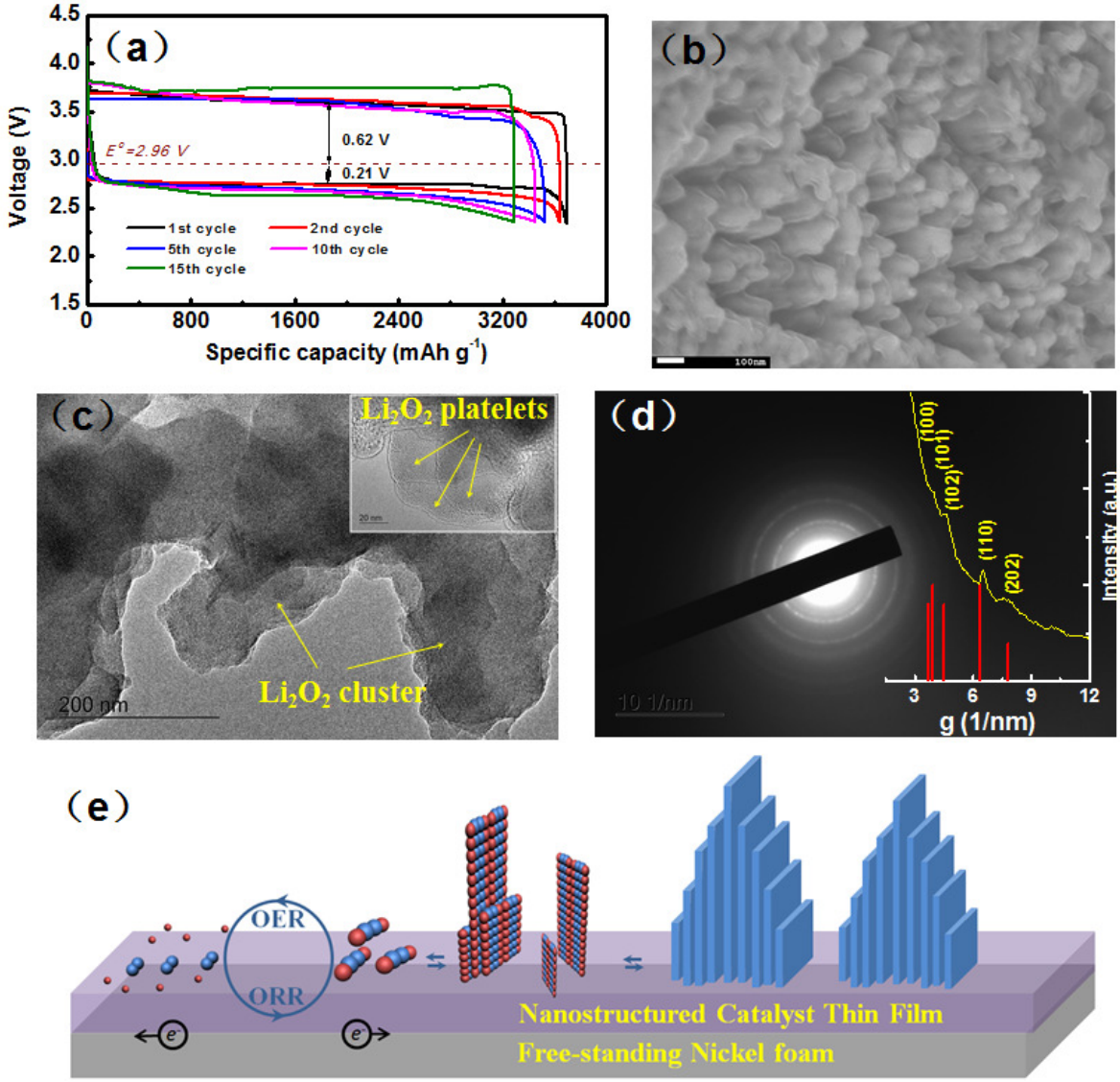

Figure 3. (a) Full discharge/charge curves for selected cycles of PG-PTF at the current density of 0.05 mA cm^{-2}; (b) high resolution SEM (HRSEM) image of discharged reaction products deposited on the thin film; (c) HRTEM image of discharged reaction products deposited on the thin film, with the inset showing higher resolution; (d) SAED pattern from (c); (e) schematic diagram of mechanism of discharge/charge process.

The full discharge capacity and overpotential results from previously published works on cathode electrocatalysts are shown in Fig. 4, including metal oxide, alloy, and precious metal nanoparticles used as electrocatalysts. Although different current densities are used, we can roughly reach the conclusion that air electrode with porous nanostructure always exhibits a

high full discharge capacity. That is because porous nanostructure leading to high surface area can provide sufficient space for reaction product deposition. [23, 36-38] In other words, passivation of activity sites from massive deposits of insulating reaction product is likely to lead to premature cell death, which will further result in large polarization and unsatisfactory cycling performance. [32, 35] Precious-metal-based electrocatalyst shows a lower overpotential than metal oxide and carbon materials, which may be the result of the highly efficient activity. [4, 10, 21] There were also many efforts made to design a carbon-free cathode or ionic liquid electrolyte because undetermined intermediate reaction products formed from high-activity LiO_2* and electrolyte decomposition. [6, 39, 40] In our work, the carbon-free, binder-free air electrode provides a high discharge capacity together with low overpotential, resulting from both the efficient synergistic catalytic activity and the continuous 3D reaction network. It can also overcome the impedance owing to the formation of interfacial Li_2CO_3 via the reaction of lithium peroxide with carbon.

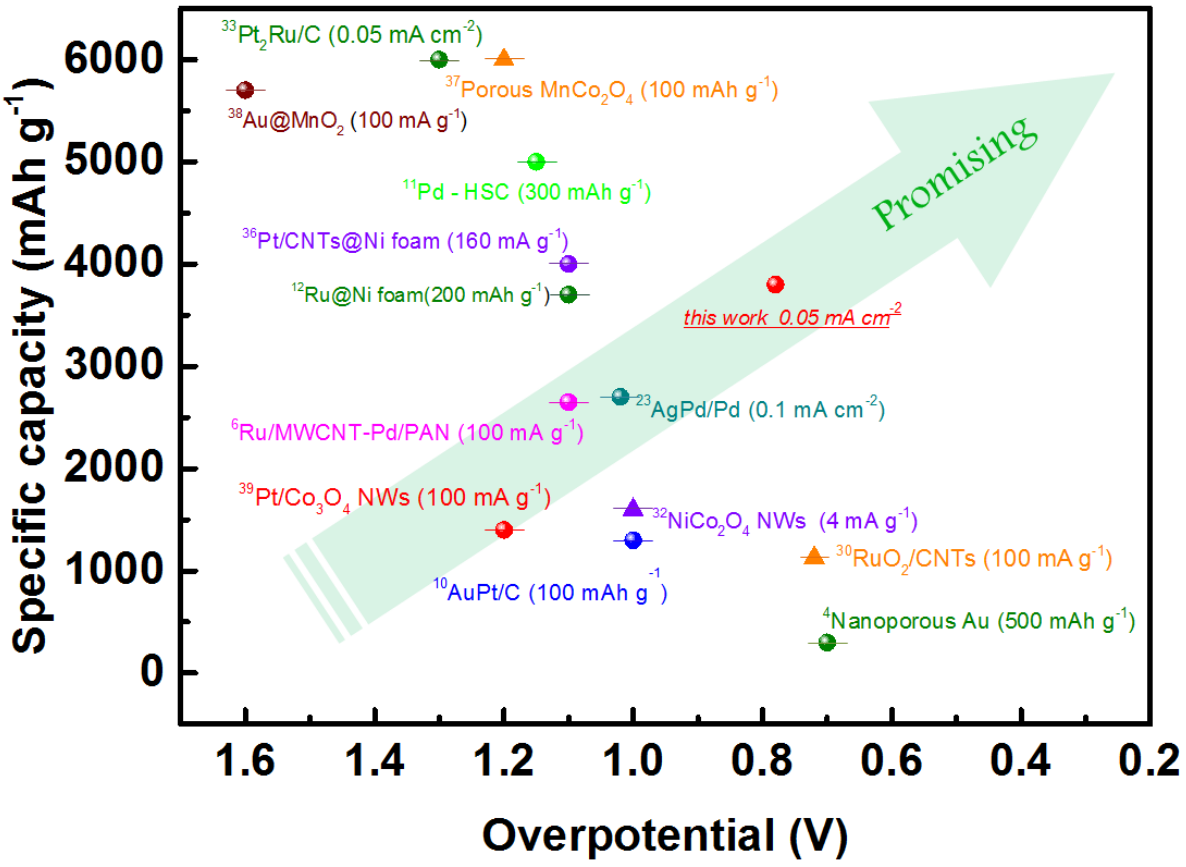

Figure 4. Full discharge capacity and overpotential results of previously published works on cathode electrocatalyst.

The cycling performance was also investigated at 0.1 mA cm^{-2} current density with a fixed specific capacity of 1000 mAh g^{-1} in Fig. 5(a, b) and Fig. S11. Compared to the Ni@P-PTF, the Ni@PG-PTF shows a high round-trip efficiency, a high ORR potential (2.62 V), and a low OER potential (3.54 V). Even after 100 cycles, the Ni@PG-PTF still exhibits a lower OER potential. In Fig. 5(b), the discharge and charge capacities retain stable values, and in addition, the discharge terminal voltage is higher than 2.5 V, while the charge terminal potential is lower than 3.7 V for 100 cycles. This excellent cycling performance can be largely attributed from the high synergistic catalytic activity of Pt-Gd. Meanwhile, the electrolyte stability was also characterized by XPS and Fourier transform infrared (FTIR) spectroscopy at different discharge/charge stages during long-term capacity-limited cycling in Fig. 5(c-e) and

Fig. S10. After the 1st discharge, there are peaks in the O 1s (Fig. 5d) and Li 1s (Fig. 5e) spectra corresponding to Li_2O_2 that are decomposed in the following charge process, which provides evidence that the reaction mechanism is consistent with the schematic representation shown in Fig. 3. In the following 40th and 80th cycles, an obvious Li_2CO_3 signal appears in the XPS spectra, as well as the appearance of a LiOH signal in the FTIR (Fig. S10). According to the published results, ether-based electrolyte is prone to autoxidation from oxygenated radicals, and decomposition occurs above 4 V, leading to the formation of non-reversible reaction products. [41, 24] Although TEGDME solvent is more stable than other organic solvents, such as in carbonate-based electrolytes, and the charge potential in this work is lower than 4 V, a mixture of non-reversible reaction products was formed, largely resulting from the electrolyte instability against high-activity oxygenated radical attack during the reaction process.

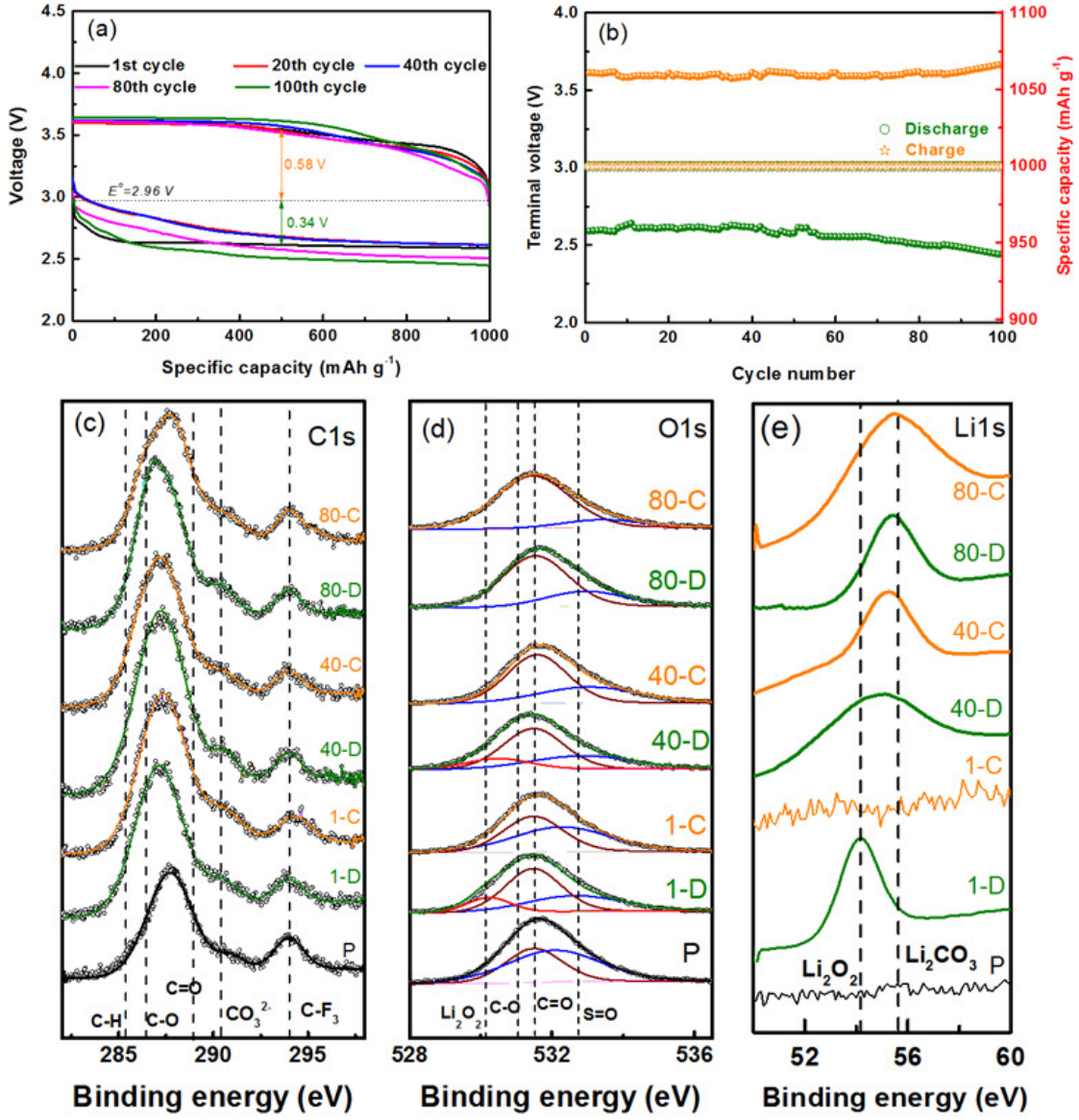

Figure 5. (a) Discharge/charge curves of PG-PTF for selected cycles; (b) cycling performance of the PG-PTF; XPS spectra of (c) C 1s, (d) O 1s, and (e) Li 1s signals from PG-PTF at different cycles.

P : electrode before discharge; 1-D : after 1st discharge; 1-C : after 1st cycle.

3. Conclusion

In conclusion, Pt-Gd polycrystalline thin film synthesized by pulsed laser deposition (PLD) exhibits excellent oxygen catalytic activity, owing to the highly efficient Pt-Gd alloy synergistic catalyst activity together with its special polycrystalline structure. Carbon-free, binder-free, air-electrode Pt-Gd alloy polycrystalline thin film on nickel foam was also used

as an air electrode. It shows favorable electrocatalyst performance, with a high round-trip efficiency in the full discharge/charge model, owing to the high catalytic activity of the Pt-Gd alloy composite and 3D porous nickel foam structure. Meanwhile, depositing high-efficient electrocatalyst on porous substrate with polycrystalline thin film by PLD is also a promising technique in the future lithium oxygen batteries research.

4. Experimental Section

Sample preparation: The targets were made by sintering a pressed mixture of platinum powder (< 40 nm, Sigma) and gadolinium powder (-40 mesh, Sigma) according to the element stoichiometry at 700 ^{o}C for 6 hours in argon gas. The laser outputs 248 nm wavelength, 30 nanosecond pulses at a frequency that may be chosen between 1 and 10 Hz. The energy of this pulse is determined by choosing the pumping high voltage (HV) of the laser. The laser HV ranges from 24 kV to 32 kV and, depending on the state of the gas medium, will produce energies in the pulse between 400 mJ and 1200 mJ. The rectangular output pulse of the laser has dimensions of approximately 30 mm × 12 mm. The substrates for deposition include nickel foam to get air electrode, TEM grids convenient for TEM operation, and glassy carbon electrode to test RDE performance.

Characterization: The morphology of the samples was examined using field emission scanning electron microscopy (FE-SEM; JEOL JSM-7500). Transmission electron microscopy (TEM) investigations were performed using a 200 kV JEOL 2011 instrument to research the thickness of the thin film. Scanning transmission electron microscopy (STEM) and elemental mapping analysis of the thin film were conducted by atomic resolution analytical microscope (ARM) investigations performed using a 200 kV JEOL 2011 instrument. The phase structures of the thin films were also analysed by selected area electron

diffraction (SAED) using a 200 kV JEOL 2011 instrument. Fourier transform infrared (FT-IR) spectra were collected using a FTIR Prestige-21 (Shimadzu). X-ray photoelectron spectroscopy (XPS) experiments were carried out on a VG Scientific ESCALAB 2201XL instrument using aluminium Kα X-ray radiation. XPS spectral analysis was conducted using XPS Peak-fit software.

Catalyst and electrochemical performance: Rotating disk electrode (RDE) aqueous electrochemical tests were carried out using a computer-controlled potentiostat (Princeton 2273 and 616, Princeton Applied Research) with a typical three-electrode cell. The working electrodes were prepared by depositing a thin film of the composite on glassy carbon electrode. Platinum foil was used as the counter electrode, and an Ag/AgCl (saturated KCl filled) electrode was used as the reference electrode. The detailed kinetic analysis was conducted according to the Koutecky-Levich (K-L) plots:

$$\frac{1}{j} = \frac{1}{j_k} + \frac{1}{B\omega^{0.5}} \quad (1)$$

where j_k is the kinetic current and B is the Levich slope, which is given by:

$$B = 0.2nF(D_{O_2})^{2/3} v^{-1/6} C_{O_2} \quad (2)$$

Here, n is the number of electrons transferred in the reduction of one O_2 molecule, F is the Faraday constant (F = 96485 C/mol), D_{O2} is the diffusion coefficient of O_2 ($D_{O2} = 1.9 \times 10^{-5}$ cm^2 s^{-1}), v is the kinematic viscosity for KOH (v = 0.01 cm^2 s^{-1},) and C_{O2} is the concentration of O_2 in the solution ($C_{O2} = 1.2 \times 10^{-6}$ mol cm^{-3}). The constant 0.2 is adopted when the rotation speed is expressed in rpm. According to Equations (1) and (2), the number of electrons transferred (n) can be obtained from the slope of the Koutecky-Levich plot of j^{-1} vs. $\omega^{-1/2}$. The non-aqueous electrochemical oxygen reduction reaction (ORR) and oxygen evolution reaction (OER) tests were carried out using computer-controlled potentiostats (Princeton 2273) in a three-electrode system. 1 M $LiCF_3SO_3$ in tetraethylene glycol dimethyl

ether (TEGDME) was used as electrolyte. The details of assembling the testing system and electrode preparation can be found in our reported work.[23] Polarization curves were obtained from open voltage to the set potential. The above procedure was repeated for each sample. In detail, argon was induced into the electrolyte for 30 min to ensure that the background data was measured in an inert atmosphere. Then, pure oxygen was purged into the electrolyte for 30 min to study the ORR. Solid dried lithium peroxide powder was added to the electrolytic cell while stirring before use for the OER study.

The electrochemical performance was tested under flowing oxygen. The working electrode was nickel foam with the catalyst deposited as a thin film. Typical loadings of cathode powder were ~1 mg cm^{-2}. The electrolyte consisted of a solution of 1 M $LiCF_3SO_3$ in TEGDME. Pure lithium foil was used as the counter electrode. The cells were assembled in an argon-filled glove-box (Mbraun, Unilab, Germany). Galvanostatic deep, full charge-discharge curves were collected at various current densities of 0.05 and 0.2 mA cm^{-2} with 2.5 V vs. Li/Li^+ discharge terminal voltage. Capacity limited charge-discharge curves were collected at current density of 0.1 mA cm^{-2}. All tests were conducted on LAND CT 2001A multi-channel battery testers at room temperature in oxygen atmosphere, using our designed facility.

Supporting Information.

Experiment details, XPS, SEM, TEM, EDS, FTIR and more electrochemical data including RDE, Charge/discharge curves. Supporting Information is available from the Wiley Online Library or from the author.

Acknowledgements

This work is supported by the Australian Research Council (ARC) through a Discovery Project (DP140100401). The authors would like to also thank Dr Tania Silver for critical reading of the manuscript, and also acknowledge the use of the facilities in the UOW Electron Microscopy Center, with particular thanks to Dr. Gilberto Casillas-Garcia. The manuscript was written through contributions of all authors. All authors have given approval to the final version of the manuscript.

Received: ((will be filled in by the editorial staff))

Revised: ((will be filled in by the editorial staff))

Published online: ((will be filled in by the editorial staff))

[1] P. G. Bruce, S. A. Freunberger, L. J. Hardwick and J. M. Tarascon, *Nat Mater*. **2012**, 11, 19.

[2] R. Black, B. Adams and L. F. Nazar, *Adv Energy Mater*. **2012**, 2, 801.

[3] L. Grande, E. Paillard, J. Hassoun, J. B. Park, Y. J. Lee, Y. K. Sun, S. Passerini and B. Scrosati, *Adv Mater*. **2015**, 27, 784.

[4] Z. Q. Peng, S. A. Freunberger, Y. H. Chen and P. G. Bruce, *Science*. **2012**, 337, 563.

[5] D. Wu, Z. Guo, X. Yin, Q. Pang, B. Tu, L. Zhang, Y. G. Wang and Q. Li, *Adv Mater*. **2014**, 26, 3258.

[6] W. H. Ryu, F. S. Gittleson, M. Schwab, T. Goh and A. D. Taylor, *Nano Lett*. **2015**, 15, 434.

[7] R. Black, J. H. Lee, B. Adams, C. A. Mims and L. F. Nazar, *Angew Chem Int Edit.* **2013**, 52, 392.

[8] F. J. Li, Y. Chen, D. M. Tang, Z. L. Jian, C. Liu, D. Golberg, A. Yamada and H. S. Zhou, *Energ Environ Sci*. **2014**, 7, 1648.

[9] W. B. Luo, S. L. Chou, J. Z. Wang, Y. C. Zhai and H. K. Liu, *Small*. **2015**,11, 2817.

[10] Y. C. Lu, Z. C. Xu, H. A. Gasteiger, S. Chen, K. Hamad-Schifferli and Y. Shao-Horn, *J*

Am Chem Soc. **2010**, 132, 12170.

[11] J. J. Xu, Z. L. Wang, D. Xu, L. L. Zhang and X. B. Zhang, *Nat Commun*. **2013**, 4, 2438.

[12] K. M. Liao, T. Zhang, Y. Q. Wang, F. J. Li, Z. L. Jian, H. J. Yu and H. S. Zhou, *Chemsuschem*. **2015**, 8, 1429.

[13] Q. C. Liu, L. Li, J. J. Xu, Z.-W. Chang, D. Xu, Y. B. Yin, X.-Y. Yang, T. Liu, Y.-S. Jiang, J. M. Yan and X.-B. Zhang, *Adv Mater*, **2015**, 27, 8095.

[14] J. J. Xu, D. Xu, Z. L. Wang, H. G. Wang, L. L. Zhang and X. B. Zhang, *Angewandte Chemie International Edition*, **2013**, 52, 3887.

[15] M. Escudero-Escribano, A. Verdaguer-Casadevall, P. Malacrida, U. Gronbjerg, B. P. Knudsen, A. K. Jepsen, J. Rossmeisl, I. E. L. Stephens and I. Chorkendorff, *J Am Chem Soc*. **2012**, 134, 16476.

[16] P. Hernandez-Fernandez, F. Masini, D. N. McCarthy, C. E. Strebel, D. Friebel, D. Deiana, P. Malacrida, A. Nierhoff, A. Bodin, A. M. Wise, J. H. Nielsen, T. W. Hansen, A. Nilsson, I. E. L. Stephens and I. Chorkendorff, *Nat Chem*. **2014**, 6, 732.

[17] I. E. L. Stephens, A. S. Bondarenko, U. Gronbjerg, J. Rossmeisl and I. Chorkendorff, *Energ Environ Sci*. **2012**, 5, 6744.

[18] S. Chen, P. J. Ferreira, W. C. Sheng, N. Yabuuchi, L. F. Allard and Y. Shao-Horn, *J Am Chem Soc*. **2008**, 130, 13818.

[19] C. H. Cui, L. Gan, H. H. Li, S. H. Yu, M. Heggen and P. Strasser, *Nano Lett*. **2012**, 12, 5885.

[20] V. R. Stamenkovic, B. Fowler, B. S. Mun, G. F. Wang, P. N. Ross, C. A. Lucas and N. M. Markovic, *Science*. **2007**, 315, 493.

[21] V. R. Stamenkovic, B. S. Mun, K. J. J. Mayrhofer, P. N. Ross and N. M. Markovic, *J Am Chem Soc*. **2006**, 128, 8813.

[22] GreeleyJ, I. E. L. Stephens, A. S. Bondarenko, T. P. Johansson, H. A. Hansen, T. F.

Jaramillo, RossmeislJ, ChorkendorffI and J. K. Nørskov, *Nat Chem*. **2009**, 1, 552.

[23] W. B. Luo, X. W. Gao, S. L. Chou, J. Z. Wang and H. K. Liu, *Adv Mater*. **2015**, 27, 6862.

[24] S. A. Freunberger, Y. H. Chen, N. E. Drewett, L. J. Hardwick, F. Barde and P. G. Bruce, *Angew Chem Int Edit*. **2011**, 50, 8609.

[25] M. M. O. Thotiyl, S. A. Freunberger, Z. Q. Peng and P. G. Bruce, *J Am Chem Soc*. **2013**, 135, 494.

[26] D. F. van der Vliet, C. Wang, D. Tripkovic, D. Strmcnik, X. F. Zhang, M. K. Debe, R. T. Atanasoski, N. M. Markovic and V. R. Stamenkovic, *Nat Mater*. **2012**, 11, 1051.

[27] J. Januschewsky, M. Ahrens, A. Opitz, F. Kubel and J. Fleig, *Adv Funct Mater*. **2009**, 19, 3151.

[28] S. J. Yoo, K. S. Lee, S. J. Hwang, Y. H. Cho, S. K. Kim, J. W. Yun, Y. E. Sung and T. H. Lim, *Int J Hydrogen Energ*. **2012**, 37, 9758.

[29] J. X. Wang, H. Inada, L. J. Wu, Y. M. Zhu, Y. M. Choi, P. Liu, W. P. Zhou and R. R. Adzic, *J Am Chem Soc*. **2009**, 131, 17298.

[30] Z. L. Jian, P. Liu, F. J. Li, P. He, X. W. Guo, M. W. Chen and H. S. Zhou, *Angew Chem Int Edit*. **2014**, 53, 442.

[31] J. Lu, L. Cheng, K. C. Lau, E. Tyo, X. Luo, J. Wen, D. Miller, R. S. Assary, H.-H. Wang, P. Redfern, H. Wu, J.-B. Park, Y.-K. Sun, S. Vajda, K. Amine and L. A. Curtiss, *Nat Commun*. **2014**, 5,4895.

[32] W. M. Liu, T. T. Gao, Y. Yang, Q. Sun and Z. W. Fu, *Phys Chem Chem Phys*. **2013**, 15, 15806.

[33] Y. Yang, W. Liu, Y. M. Wang, X. C. Wang, L. Xiao, J. T. Lu and L. Zhuang, *Phys Chem Chem Phys*. **2014**, 16, 20618.

[34] Q. C. Liu, J. J. Xu, D. Xu and X. B. Zhang, *Nat Commun*, **2015**, 6, 7892.

[35] J. J. Xu, Z. L. Wang, D. Xu, F. Z. Meng and X. B. Zhang, *Energ Environ Sci*, **2014**, 7,

2213.

[36] J. X. Li, Y. Zhao, M. Z. Zou, C. X. Wu, Z. G. Huang and L. H. Guan, *Acs Appl Mater Inter*. **2014**, 6, 12479.

[37] S. C. Ma, L. Q. Sun, L. N. Cong, X. G. Gao, C. Yao, X. Guo, L. H. Tai, P. Mei, Y. P. Zeng, H. M. Xie and R. S. Wang, *J Phys Chem C*. **2013**, 117, 25890.

[38] M. H. Lu, J. L. Qu, Q. F. Yao, C. H. Xu, Y. Zhan, J. P. Xie and J. Y. Lee, *Acs Appl Mater Inter*. **2015**, 7, 5488.

[39] J. Y. Cao, S. Y. Liu, J. Xie, S. C. Zhang, G. S. Cao and X. B. Zhao, *Acs Catal*. **2015**, 5, 241.

[40] G. A. Elia, J. Hassoun, W. J. Kwak, Y. K. Sun, B. Scrosati, F. Mueller, D. Bresser, S. Passerini, P. Oberhumer, N. Tsiouvaras and J. Reiter, *Nano Lett*. **2014**, 14, 6572.

[41] B. D. McCloskey, R. Scheffler, A. Speidel, D. S. Bethune, R. M. Shelby and A. C. Luntz, *J Am Chem Soc*. **2011**, 133, 18038.

Supporting Information

Binder-free and carbon-free 3D porous air electrode with high capacity, high efficiency, and long life for Li-O_2 batteries

Wen-Bin Luo, Xuan-Wen Gao, Dong-Qi Shi, Shu-Lei Chou, Jia-Zhao Wang*, Hua-Kun Liu*

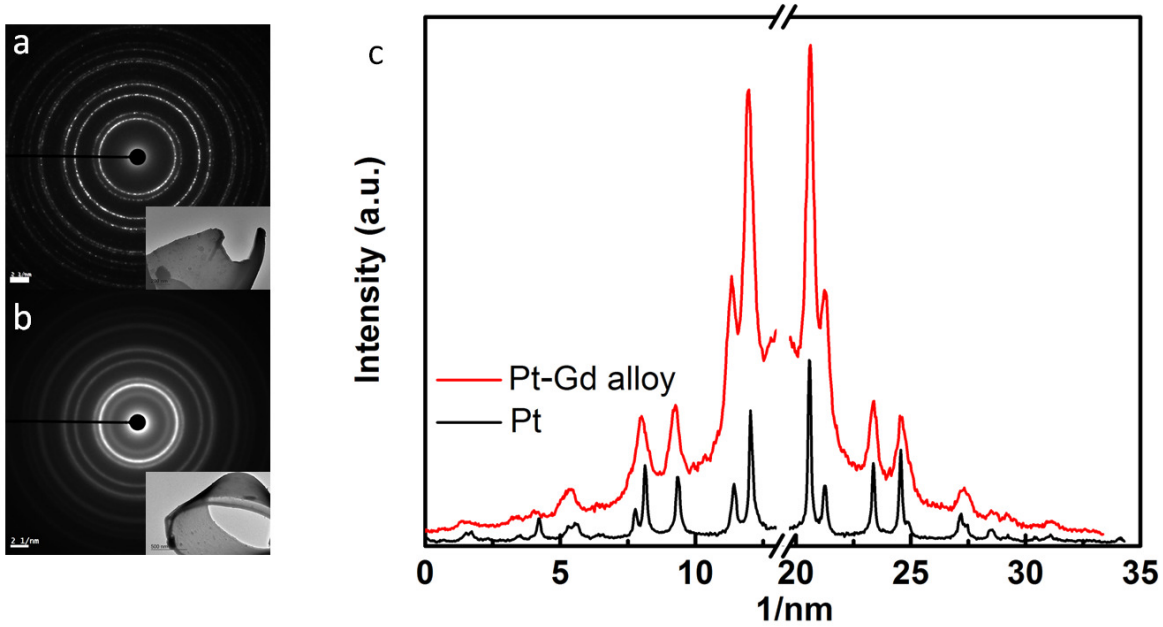

Figure S1. SAED patterns of P-PTF (a) PG-PTF (b); (c) SAED pattern comparison of P-PTF and PG-PTF, data from (a), (b).

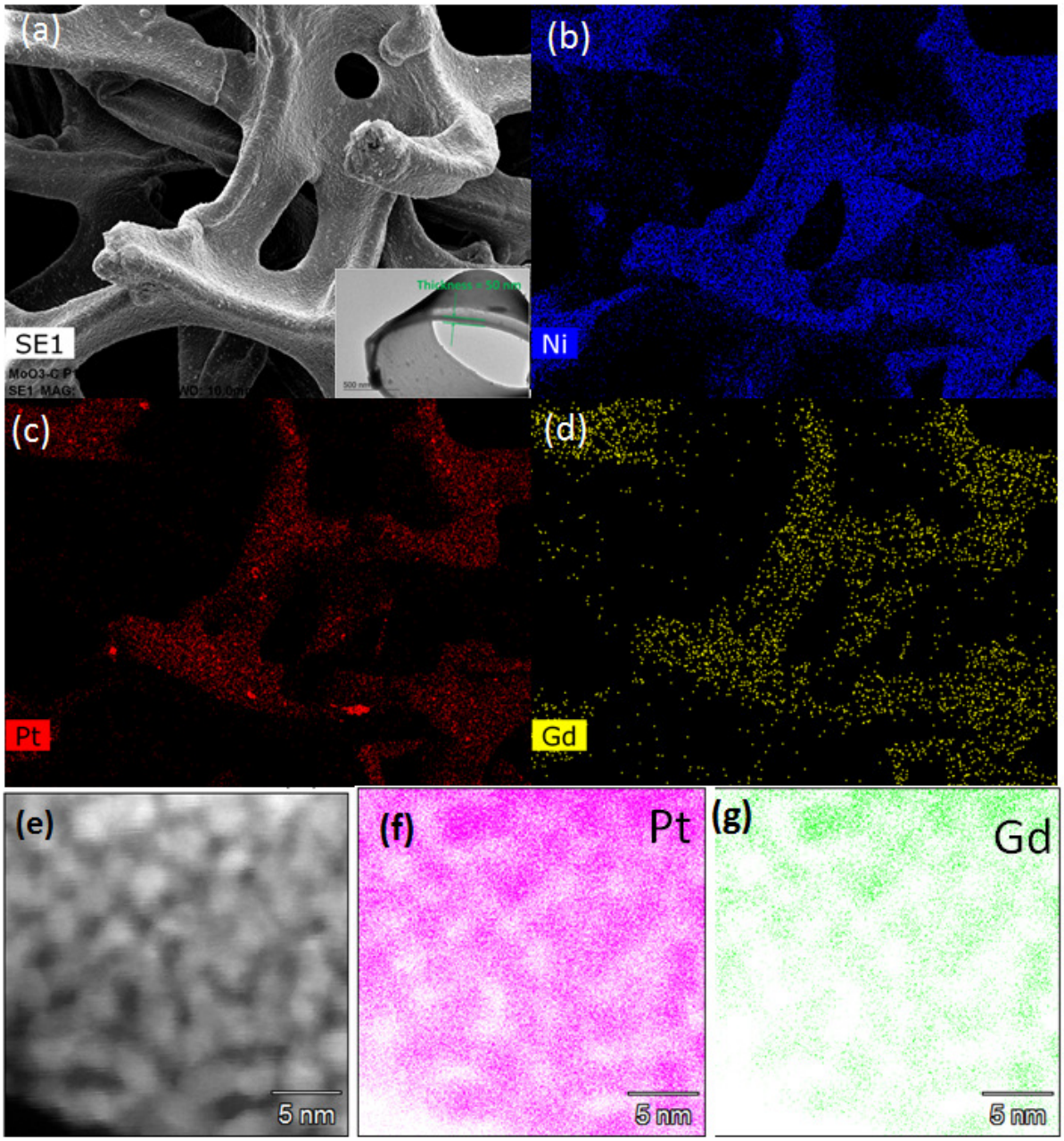

Figure S2. (a) FESEM of Ni@PG-PTF air electrodes,(inset showing the HRTEM of Pt-Gd alloy PTF at higher magnification); elements distribution spectrum of (b) Ni; (c) Pt and (d) Gd obtained from (a); Pt and Gd elements distribution in Pt-Gd alloy thin film tested by STEM (e-g).

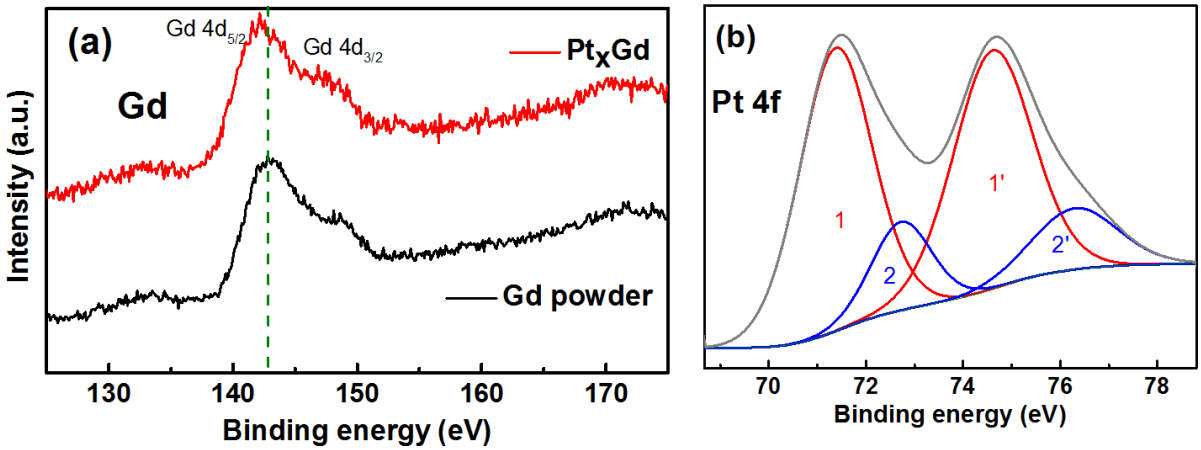

Figure S3. XPS spectra of Gd (a) and Pt (b) of de-alloying Pt-Gd alloy composite.

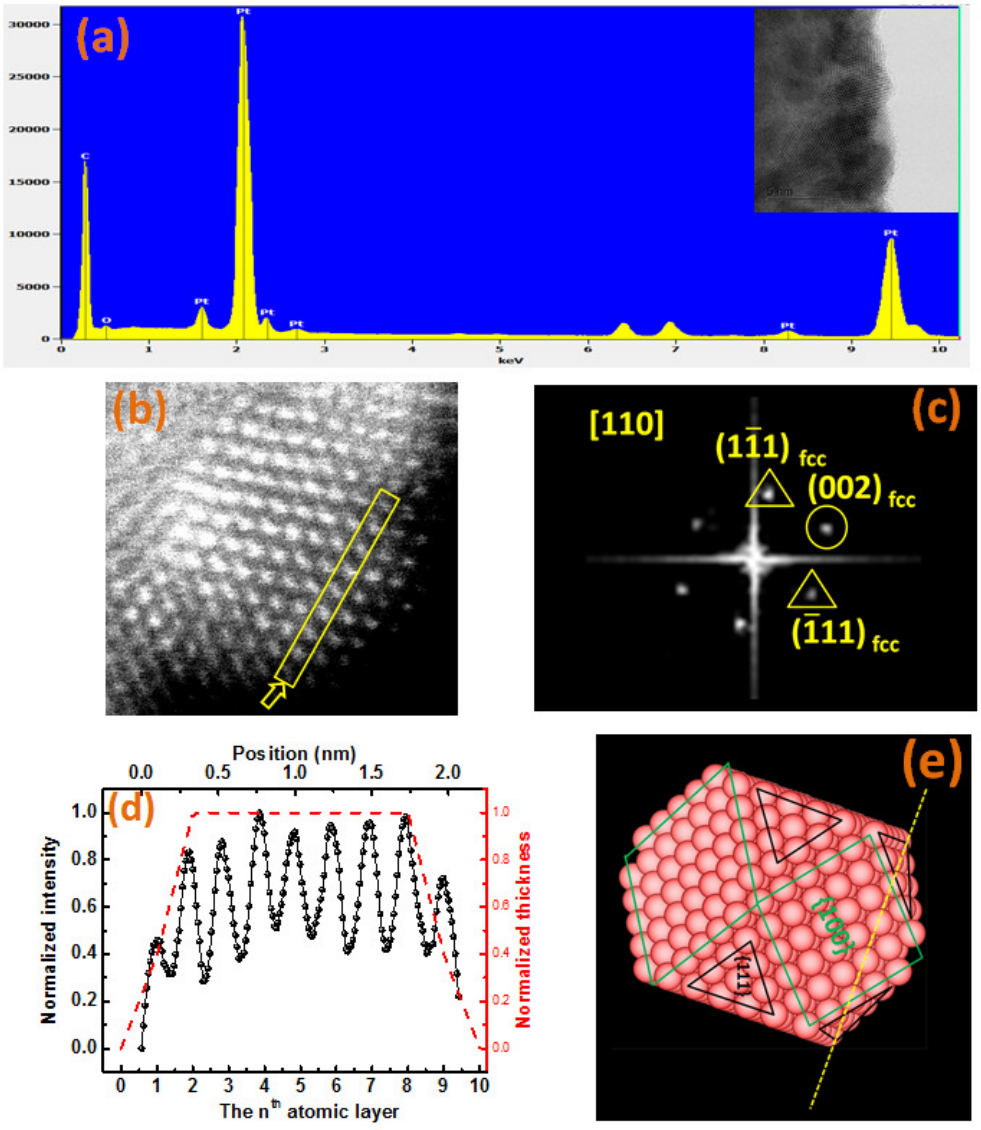

Figure S4. (a) EDS spectrum of P-PTF obtained from the area inset; (b) aberration-corrected HAADF image of Pt nanoparticle; (c) fast Fourier transform (FFT) pattern of Pt nanoparticle in (b); (d) normalized image intensity of the particle in (b) along the atoms in theyellow rectangle (solid curve), with the dashed curve showing the normalized thickness changes obtained by assuming the shape of an ideal nanoparticle as shown in (e).

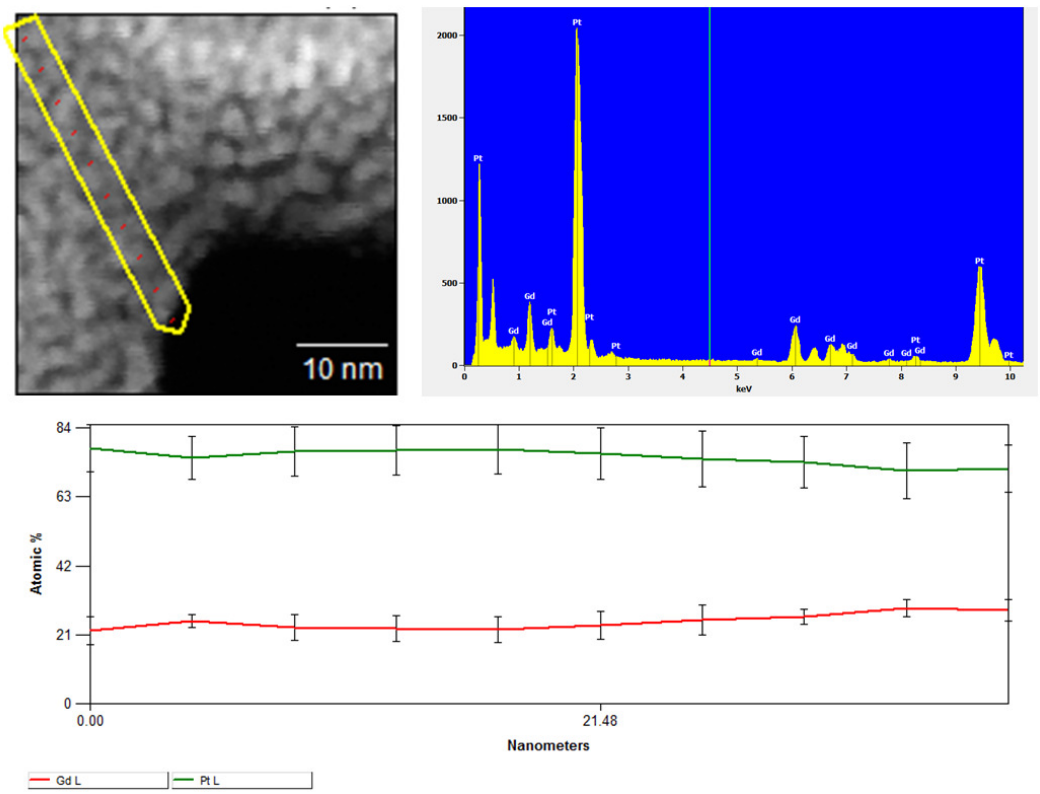

Figure S5. Element distribution of PG-PTF.

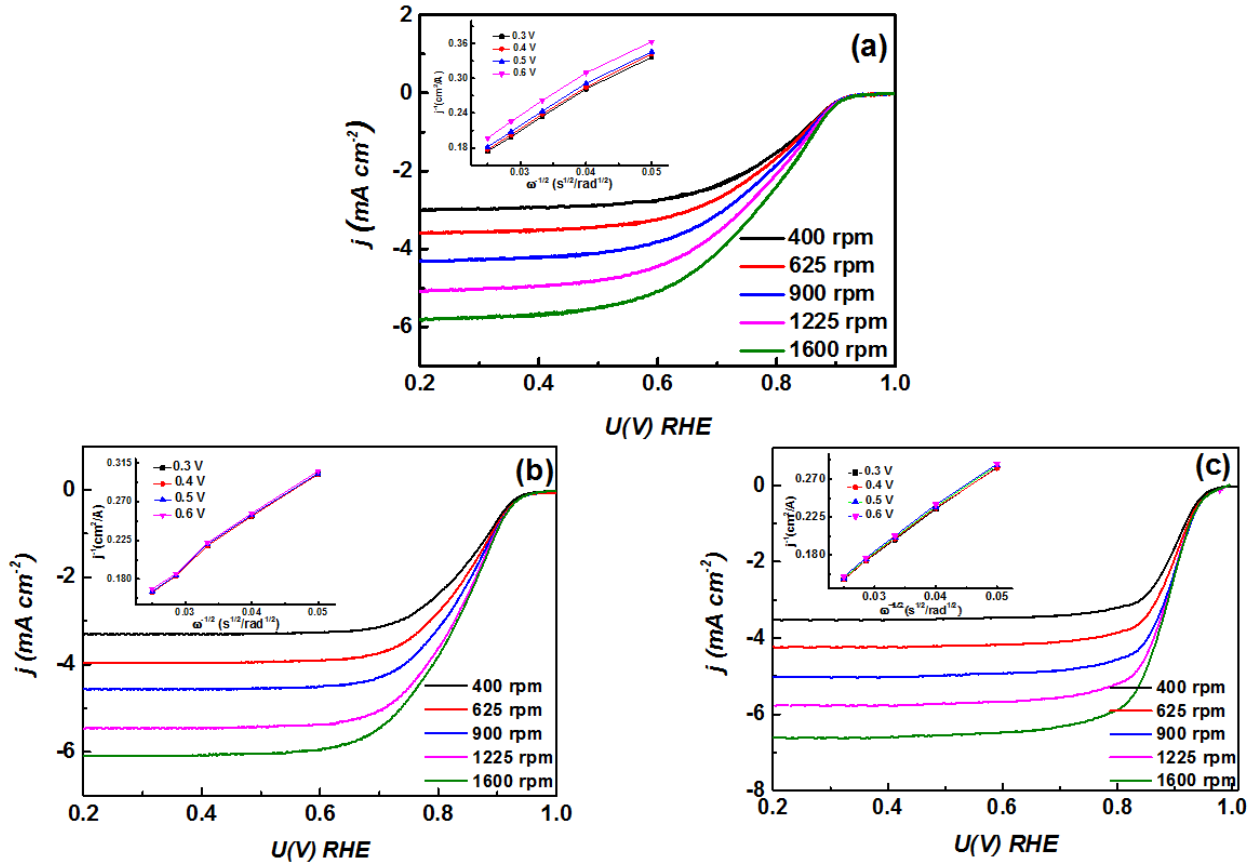

Figure S6. RDE curves of commercial Pt electrode (a); P-PTF (b); and PG-PTF in O_2-saturated 0.1 M KOH solution (c) with various rotation speeds and a sweep rate of 10 mV s^{-1}; insets show corresponding K–L plots (J^{-1} versus $\omega^{-1/2}$) at different potentials. RHE: reversible hydrogen electrode.

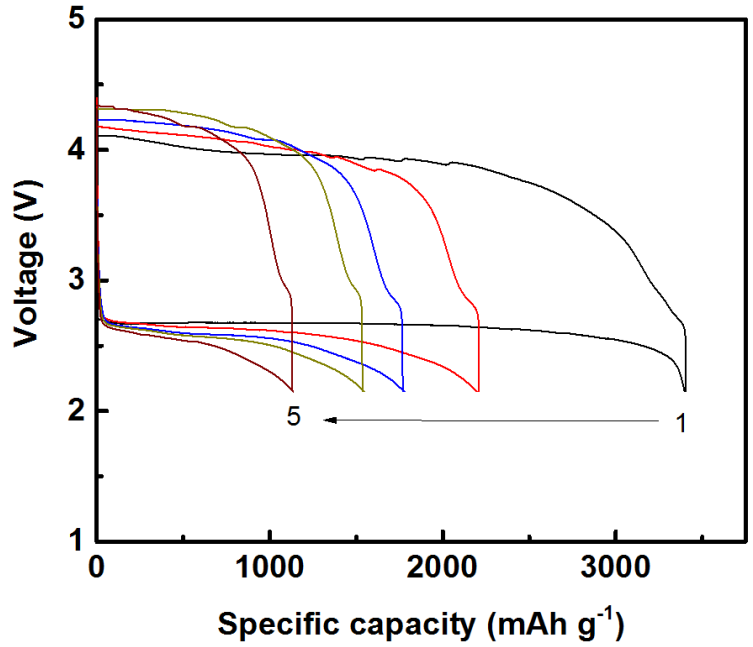

Figure S7. Full discharge/charge curves for the first 5 cycles of P-PTF at the current density of 0.05 mA cm^{-2}.

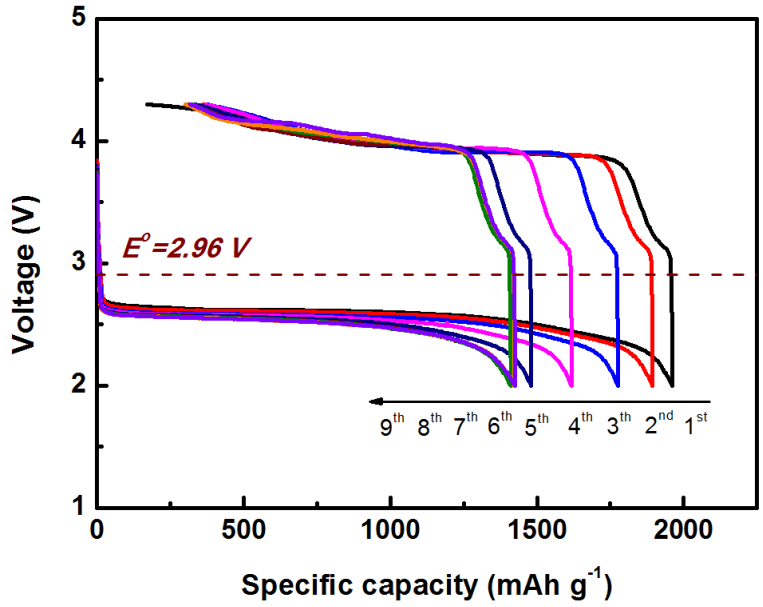

Figure S8. Full discharge/charge curves for the first 9 cycles of PG-PTF at the current density of 0.2 mA cm^{-2}.

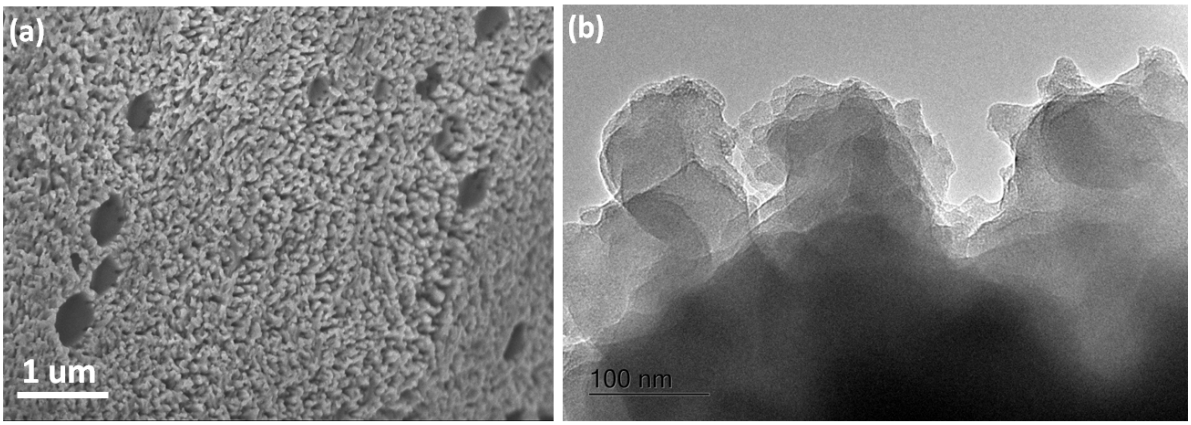

Figure S9. FESEM (a) and HRTEM (b) images of discharged reaction products deposited on the thin film.

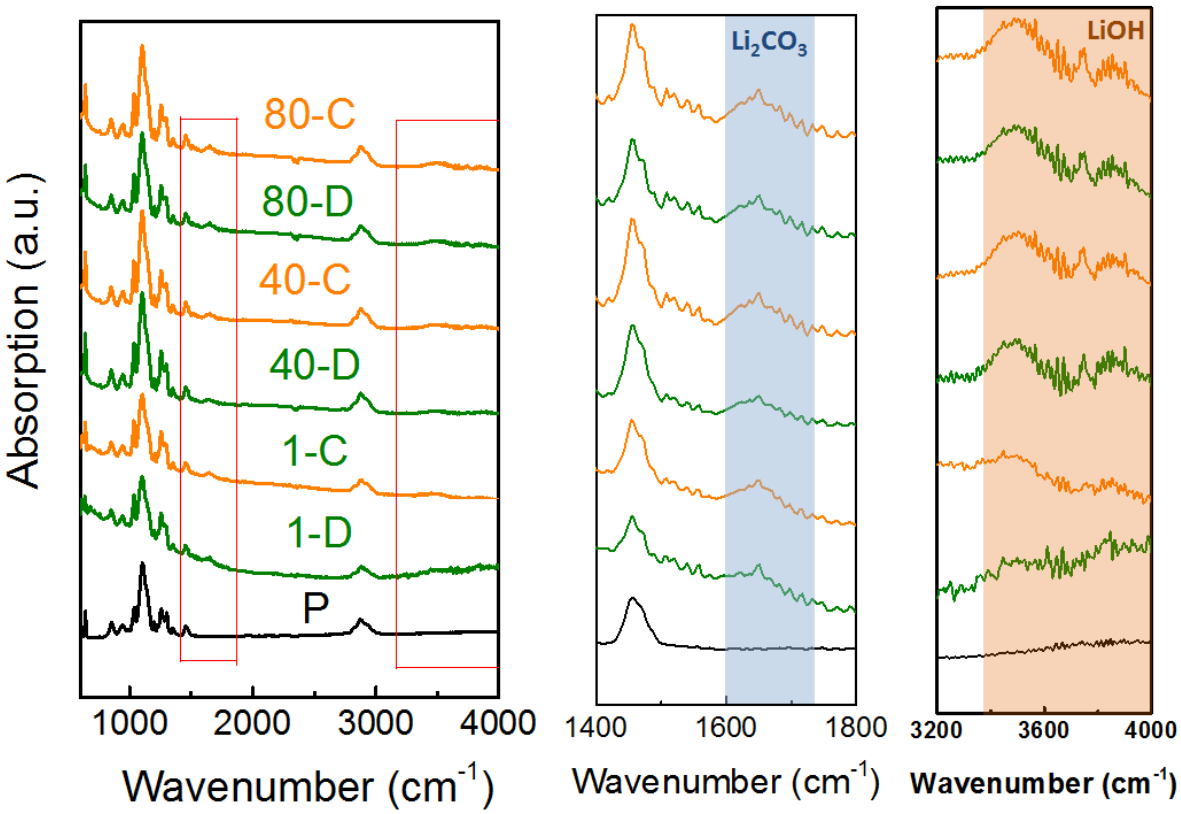

Figure S10. FTIR curves of air electrode at different cycles.
P : electrode before discharge; 1-D : after 1st discharge; 1-C : after 1st cycle.

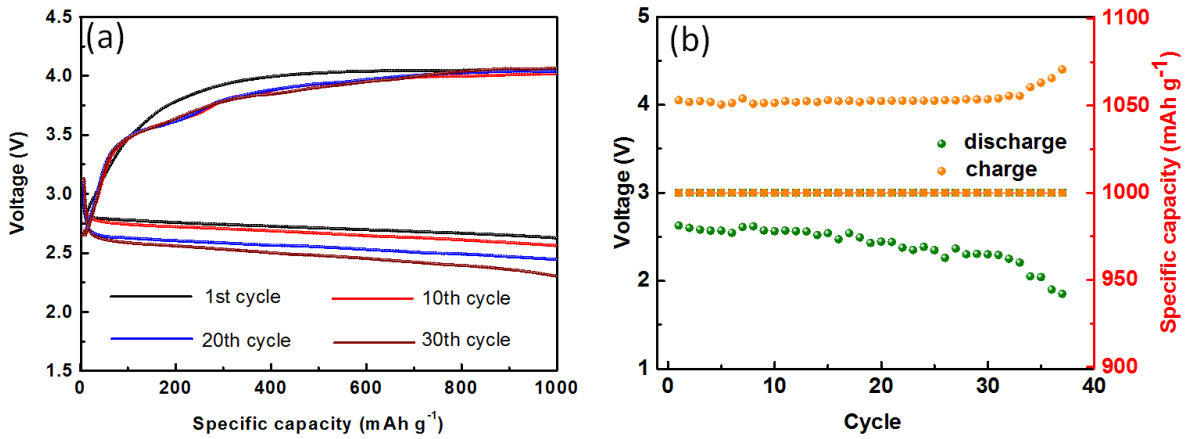

Figure S11. (a) Discharge/charge curves of P-PTF for selected cycles; (b) cycling performance of the P-PTF.